RESEARCH ARTICLE | DECEMBER 24 2024

# Tracking of atomic planes in atom probe tomography

Sebastian Koelling ; Simone Assali ; Guillaume Nadal ; Dieter Isheim ; David N. Seidman ; Oussama Moutanabbir



*J. Appl. Phys.* 136, 245103 (2024)
https://doi.org/10.1063/5.0226890

Journal of Applied Physics METHOD pubs.aip.org/aip/jap

# Tracking of atomic planes in atom probe tomography

Cite as: J. Appl. Phys. **136**, 245103 (2024); doi: 10.1063/5.0226890
Submitted: 11 July 2024 · Accepted: 4 December 2024 ·
Published Online: 24 December 2024



Sebastian Koelling,[1,a)] Simone Assali,[1] Guillaume Nadal,[1] Dieter Isheim,[2] David N. Seidman,[2] and Oussama Moutanabbir[1]

## AFFILIATIONS

[1]Department of Engineering Physics, École Polytechnique de Montréal, C. P. 6079, Succ. Centre-Ville, Montréal, Quebec H3C 3A7, Canada
[2]Department of Materials Science & Engineering and Northwestern University Center for Atom Probe Tomography (NUCAPT), Northwestern University, Evanston, Illinois 60208, USA

[a)]**Author to whom correspondence should be addressed:** sebastian.koelling@polymtl.ca

## ABSTRACT

Atom probe tomography is a ubiquitous method in materials science and engineering capable of revealing the atomic-level three-dimensional composition of a plethora of materials. Beside the nature of atoms forming the analyzed material, atom probe data are also known to contain information on the crystallography. In particular, remnants of the atomic plane sets forming on the surface of the tip-shaped samples are commonly found in atom probe data sets of crystalline metallic materials. The plane remnants can be utilized to correlate the nano-scale chemical analysis that atom probe tomography provides with the crystallographic structure on the same scale. We describe a protocol to reveal and track the atomic planes systematically from raw atom probe data. We demonstrate for both metals and semiconductors that the extracted crystallographic can be used to calibrate a dynamic reconstruction of the respective data set acquired in atom probe tomography. Furthermore, we utilize the crystal planes to make precise measurements of layer thicknesses in atom probe data of semiconductor heterostructures.





## INTRODUCTION

Understanding the formation of crystals and controlling the arrangement of crystallites in three-dimensions is profoundly important for the progress in materials science.[1–3] Hence, the development of materials is going hand in hand with the development of sophisticated microscopy tools and techniques to accurately investigate the structure of the materials across many length scales down to the atomic scale.[4–8]

Progress in electron tomography,[6] coherent x-ray imaging,[5] and atom probe tomography (APT)[7,8] have enabled the mapping of materials in three-dimensions and make it, for example, possible to reveal the relation between the arrangement of crystallites and the properties of the formed grain boundaries.[7–9]

While the tomographic data sets gathered during APT are known to contain crystallographic information, these information are usually retrieved by manually filtering the data sets based on heuristics.[10,11] This is a time consuming procedure that is unlikely to capture all plane remnants present in the data set and relies on being able to reconstruct the acquired data to a high enough standard to be able to see the plane remnants[12] without prior knowledge.

Here, a protocol is introduced that allows to automatically find and track the crystal features throughout full APT data sets containing hundreds of millions of ions. The validity of this protocol is confirmed for both a voltage-pulsed measurement of pure metal and a laser-pulsed measurement of a semiconductor heterostructure. We also demonstrate that the information extracted is highly consistent and enables the dynamic reconstruction[13] of the data sets with a sub-10 nm length for each dynamically reconstructed segment.

APT is a method to analyze the atomic constituents of a material one-by-one. It progresses by successively projecting atoms as ions from the surface of a tip-shaped sample onto a position-sensitive single ion detector.[14] During the measurement process, a tip-shaped sample is disassembled using a DC electric field superposed with field—or laser pulses to trigger the removal or

evaporation of single ions from the tip's surface. If the analyzed material is crystalline, the tip surface is known to form a steady shape that is approximately a hemispherical cap[15] dominated by atomic terraces forming where crystal planes cut the hemisphere.[16,17] If the removal of these atomic terraces progresses periodically in time during APT, remnants of the crystallographic planes are found in the reconstructed data sets.[12,18] This is a result of reconstructing the depth axis in the data set as a sum over the volume of the incoming ions.[15,19]

The imaged atomic planes can be used to inform the reconstruction of the acquired data[10] and allows for the implementation of more advanced reconstruction protocols.[13] Furthermore, a calibration of the atom probe data to the underlying crystal is needed to calibrate length scale within the reconstructed images[20] and the calibrated tomographic image of the material generated in this way allows to directly image the relation between the geometry of nanocrystallites and their grain-boundaries.[7,8]

In the following section, a detailed account of the algorithm to find and track crystal planes in volumes analyzed by APT is described. The section after that outlines the protocol that utilizes the extracted information to calculate the parameters for a dynamic reconstruction of the analyzed volume. Finally, we demonstrate that this protocol enables highly accurate thickness measurements of layers in semiconductor heterostructures.

## REVEALING STRUCTURES IN APT DATA

It is important to keep three facts about APT analyses in mind in order to understand the workings of the algorithm.

First, APT data reconstruction consists of creating a three-dimensional image from data acquired on a two-dimensional detector. The third dimension is hence not directly imaged but derived. The derivation is based on two assumptions: ions removed later during the measurement originate from a position deeper in the sample, and the volume of the analyzed region can be derived by summing over the volumes of the detected ions.[15] The volume of each type of ion is an input parameter to this process. The third dimension is then generated by summing over the volume of the detected ions in such a way that each "slab" of ions in the reconstructed volume corresponds to its ionic/atomic volume (adjusted for the detector efficiency[21]).

Second, the size of the detector in any specific APT tool is given by engineering constraints, and typically ions from the outer regions of the tip-shaped sample do not reach the detector as they fly past it or get screened by parts of the instrument. These ions cannot be used for the data reconstruction and the volume of the imaged region is adjusted, respectively.[15] However, remnants of atomic planes are found in the data set when the distances between the sets of atoms that are at the same position on subsequent atomic shells of the reconstructed tip surface are equal in the reconstructed data set. This distance is dependent on how much volume has been summed over and hence how many ions of any given volume have been detected in between these subsequent atoms in the same position of an atomic shell. If the depth axis is reconstructed by summing over all the ions arriving at the detector, the ion evaporation process over the entire tip surface imaged on the detector needs to be highly reproducible. Only a highly reproducible evaporation process, where atomic layer by atomic layer is peeled off of the entire imaged surface of the tip, ensures that the number of ions (= volume) removed in between two subsequent ions on any given set of crystal shells is always approximately the same. As a result, if the detector gets "too large" plane, remnants can disappear in the reconstructed data as irregularities in the evaporation sequence anywhere on the detector will have a detrimental effect on the ability to image plane remnants everywhere. The remnants can however be restored when the detector size is limited artificially and regions of irregular evaporation behavior are excluded from the data reconstruction. However, atom probe tools have a limited detection efficiency and if the detector size is limited too much, the statistical nature of the detection process can also introduce irregularities that are detrimental to the fidelity of the imaged remnants.

The third fact is that the ions removed from a two-dimension (hemispherical-) curved surface (the cap of a tip-shaped sample) are projected onto a flat two-dimensional surface (the detector) during APT. The shell-by-shell removal process explained in the previous paragraph then locally creates images of the crystal plane sets whose normal vector are approximately perpendicular to the hemisphere formed by the tip's surface (i.e., the set of crystal planes whose terraces form the tip surface in the specific position). Their image on the detector is however perpendicular to the detector plane and hence perpendicular to the depth axis if the reconstruction of the data does *not* account for the curvature of the tip.[22]

We can now combine these facts to build the algorithm. Using fact three, we generate a set of simple detector space reconstruction (DSR)[22] by stacking atoms along the depth axis based on their arrival sequence and volume (using fact one). Using fact two, we make each DSR only contain a subset of the data set by filtering out square-shaped neighborhoods from the detector coordinates. Now, we can expect to find almost all plane remnants along the depth axes of the DSR and hence extract them using a one-dimensional fast Fourier transformation (FFT). Note that we can create partially overlapping DSR and demand that plane remnants appear in all DSR that contain them to overcome statistical odds. This is equivalent to the postulate that a periodic signal in a neighborhood of an APT data set is a signal originating from a real crystal lattice plane in the analyzed material if all reconstructions of sufficiently large neighborhoods containing the prospective lattice plane exhibit the periodic signal.

The algorithm reduces the complicated and time consuming problem of searching for periodic structures in a three-dimensional space[23,24] to a series of one-dimensional searches that can be handled orders of magnitude more efficiently on to-date's computing hardware. Furthermore, the algorithm works in detector-space using a DSR and can hence be directly applied to raw atom probe data with no manual input or calibration needed.

The algorithm is illustrated in Fig. 1. DSR are created by filtering a small, square-shaped region of the detector [Fig. 1(a)], using the detector impact positions as x and y coordinates, and creating a z-coordinate by stacking the atoms according to the order of arrival [Fig. 1(b)]. As it is convenient for the subsequent data processing, each DSR is made to have the exact same overall z-dimension/length. Hence, each atom contributes to a certain progression of

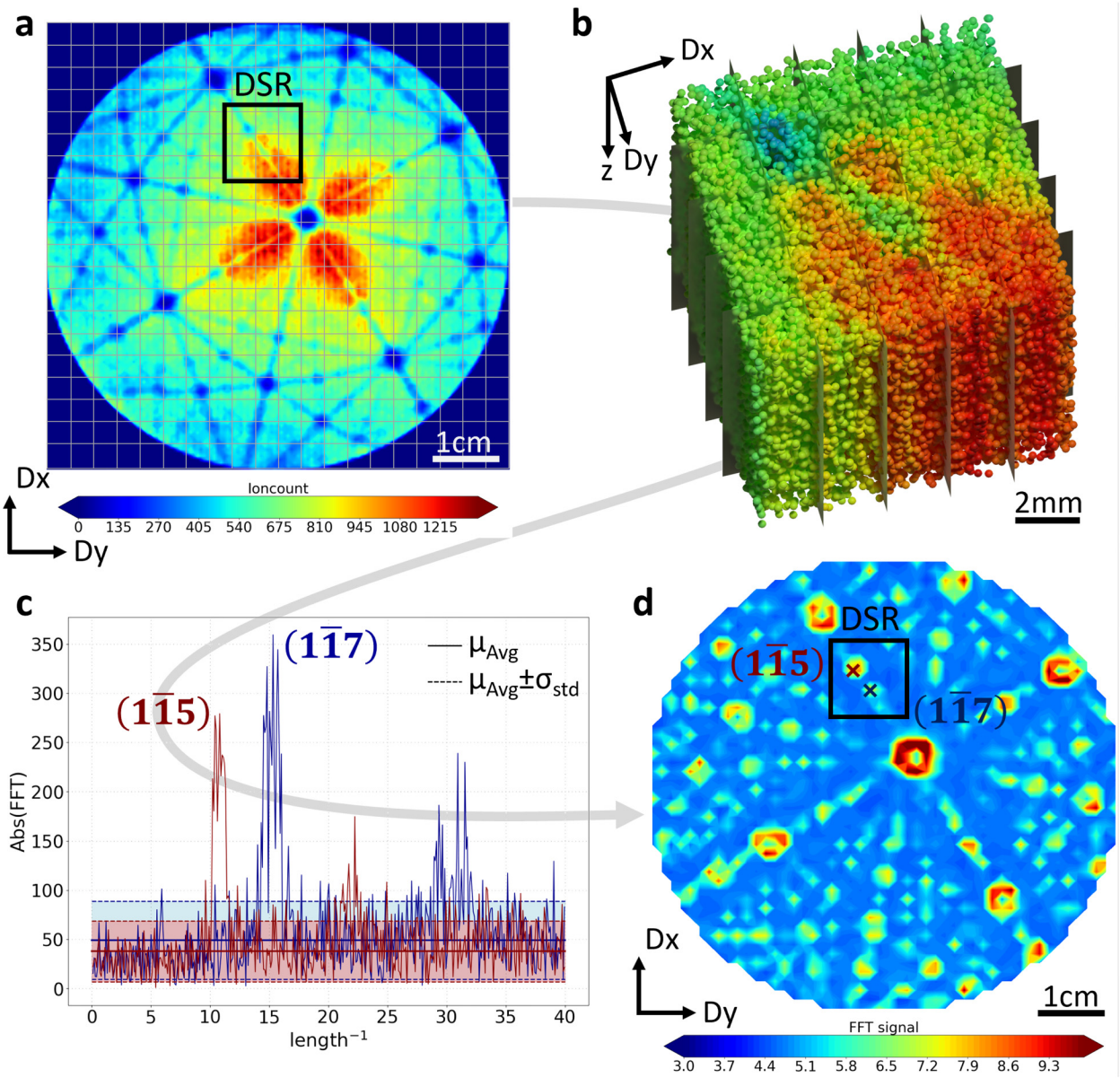


**FIG. 1.** Finding plane remnants in APT data: APT detector impact map from a pure aluminum tip (a) with a sketch of the Fourier grid used for data analysis in gray and an example window of $10 \times 10\,\mathrm{mm}^2$ used for a detector space reconstruction (DSR). The result of the DSR (b) with the Fourier grid marked by gray planes. A one-dimensional FFT of the z-coordinates of the ions in each box is used to find plane remnants. Two exemplary FFT results (c) from the boxes near the (1$\bar{1}$5) and (1$\bar{1}$7) pole, respectively, with the average Fourier intensity ($\mu_{Avg}$) shown by a full line and the range of one standard deviation ($\sigma_{std}$) highlighted. The number of standard deviations the highest peak is above the average is used as the Fourier signal. The map of the Fourier signal associated with the map in (a) is shown in (d). The same DSR window and the pixels associated with the (1$\bar{1}$5) and (1$\bar{1}$7) poles from (c) are highlighted. The map reveals the position of the remnant planes in the APT data set. A detailed analysis of 130 plane sets found in this data set is presented in Sec. S2 of the supplementary material.

the z axis via its atomic volume and after reconstructing the full set, the axis is re-scaled to the desired length.

Potential remnants of the crystal planes are now revealed using the Fast Fourier Transformations (FFT)[25] on a grid that splits the detector up into small squares [Figs. 1(b) and 1(c)]. For the detector of a Cameca LEAP 5000XS with a radius of 70 mm, we typically use square grids with $50 \times 50$ to $70 \times 70$ bins called the Fourier grid from here on. Hence, each square has a width of

1–1.4 mm. We use a 10 mm neighborhood for creating the DSR. Again, for the convenience of the subsequent data processing, the Fourier grid is fixed with respect to the detector as shown in Fig. 1(a). If a bin/square of the Fourier grid is fully inside the current DSR, the *one-dimensional* FFT of the ions inside the square is calculated using *only* the z-coordinates of the ions [Fig. 1(c)]. The global maximum of the Fourier signal excluding the peak at 0 is found and its position and signal strength are recorded for further processing.

Signal strength is defined as the number of standard deviations the peak is above the average signal in the one-dimensional Fourier space as shown in Figs. 1(c) and 1(d). Note that as the window for the DSR is moved over the detector, each bin of the Fourier grid is processed multiple times. Figure S1 (supplementary material, SM) shows an example of using $10 \times 10\,\mathrm{mm}^2$ DSR window moved by 3 mm after each reconstruction. For the settings shown in Fig. S1, this results in several 10 FFT analyses for each bin in the Fourier grid. The average position and average signal strength of these analyses result in a map revealing the crystal planes in each slice of $1-5 \times 10^6$ ions [Fig. 1(d)].

The use of the one-dimensional FFT in combination with a trivial reconstruction algorithm enables us to process in excess of $1 \times 10^6$ ions/min on a single modern processor core using code written in Python 3.11 utilizing Numpy 1.26[26] and Scipy 1.11[27] for the main data processing steps. As all DSR can be processed independently, the algorithm can be parallelized straightforwardly and data sets containing more than 100 million ions can be processed in less than an hour with current high-end desktop computers. More details on the settings used for the examples shown in the paper and the supplementary materials as well as additional information that can be extracted from the algorithm is presented in supplementary material Sec. S1.

In Fig. 2, the Fourier signal of an aluminum tip measured in a Cameca LEAP 5000XS is shown. Each spot tags a set of atomic planes on the surface of the aluminum tip. Spatial distribution maps (SDMs)[12] of selected spots show that atomic planes down to a plane spacing of 26 pm are tagged by the algorithm which is in good agreement with the expected depth resolution.[23,28] It is also demonstrated that plane sets are absent in a region where the algorithm does not tag anything. Note that in Fig. 2 all plane sets are reconstructed perpendicular to the surface of the tip mimicking the signal the algorithm "sees" when generating the map. A more detailed analysis of this data set is presented in Sec. S2 showing the presence of 130 plane sets and the spacing and angles they exhibit when reconstructed with the standard atom probe reconstruction protocol.[15] The data in Sec. S2 demonstrate that the revealed atomic planes are consistent with the well-known structure of the aluminum FCC lattice.[5,29]

The ability to find and track plane sets with a spacing of less than 0.03 nm shows the potency of this work in enhancing our understanding of the evolution of the sample surface during APT. Revealing more than 100 plane sets in an APT analysis, as demonstrated in Sec. S2, enables a detailed mapping of the surface of APT tips. The information can be used to evaluate reconstruction algorithms by evaluating how many plane sets are faithfully reconstructed based on the known angular and distance relationships between the respective plane sets.[29] Furthermore, it can be used to evaluate simulations of APT maps,[30–32] by comparing the presence and arrangement of facets on the tip surface between the measurement and the simulation.

In Fig. 3, a laser-pulsed measurement on pure Ge is presented, demonstrating the algorithms' ability to reveal plane sets in laser-pulsed APT measurements of semiconductors. In Sec. S3, a laser-pulsed measurement on $Si_{0.06}Ge_{0.90}Sn_{0.04}$ is presented and Sec. S4 a laser-pulsed measurement on silicon is presented, providing additional confirmation of the versatility of the algorithms and its relevance to the investigation of semiconductor materials and heterostructures. The analysis of the plane sets shows that the resolution of APT perpendicular to the tips' surface (commonly misnamed as depth resolution) is better than 0.03 nm in the voltage-pulsed Al analysis,[23] better than 0.08 nm in the laser-pulsed Ge analysis, better than 0.14 nm in the laser-pulsed silicon analysis and better than 0.17 nm in the laser-pulsed $Si_{0.06}Ge_{0.90}Sn_{0.04}$ analysis.

Revealing three or more plane sets is sufficient to calibrate the current standard protocol to reconstruct APT data.[10,13,15] In multicrystalline materials revealing three or more planes sets in each crystallite makes it possible to map the grain orientations.[7] In the following section, we show how the introduced algorithm can be used to extract the parameters to reconstruct an APT data set.

## EXTRACTING RECONSTRUCTION PARAMETERS

The distances and angles between crystal planes are typically well known from, e.g., x-ray diffraction experiments and theoretical considerations.[5,29] Tracking the presence of the planes throughout the volume of an APT analysis hence enables extracting the parameters needed for the data reconstruction by matching the angles and distances in the image to the theoretical values as best as possible.[10]

For the purpose of this work, we follow the reconstruction model described in Appendix C in Ref. 19. Following Ref. 19, we use an projection with angular compression to map the detector impact coordinates of the ions onto a hemispherical tip surface. To reconstruct the data set, we need to extract the evolution of the radius of the hemisphere and the image compression factor (ICF), which dictates the angular compression, using the crystal plane remnants. The ICF effectively determines the projection point of an azimuthal projection which in APT is generally somewhere between a gnomonic projection (ICF = 1) and a stereographic projection (ICF = 2).[33] The ICF is defined as a ratio between angles: the first angle being between the center of the hemisphere that models the tip surface and two points on the hemisphere's surface and the second angle being between the center of the hemisphere and the coordinates on the detector where the two surface points are projected to. The relation between a projection based on a fixed ICF and a point projection model is discussed in supplementary material Sec. S5. For data sets originating from a LEAP 5000 XS with a field of view of approximately 55°, the point projection and the angular compression model are for practical purposes identical.

With this in mind, we can now use the results of the plane detection algorithm shown in Figs. 1(d), 2, and 3 to find the reconstruction parameters for every slice of, e.g., $1-5 \times 10^6$ ions that we applied the plane search to. First, we use the position of any

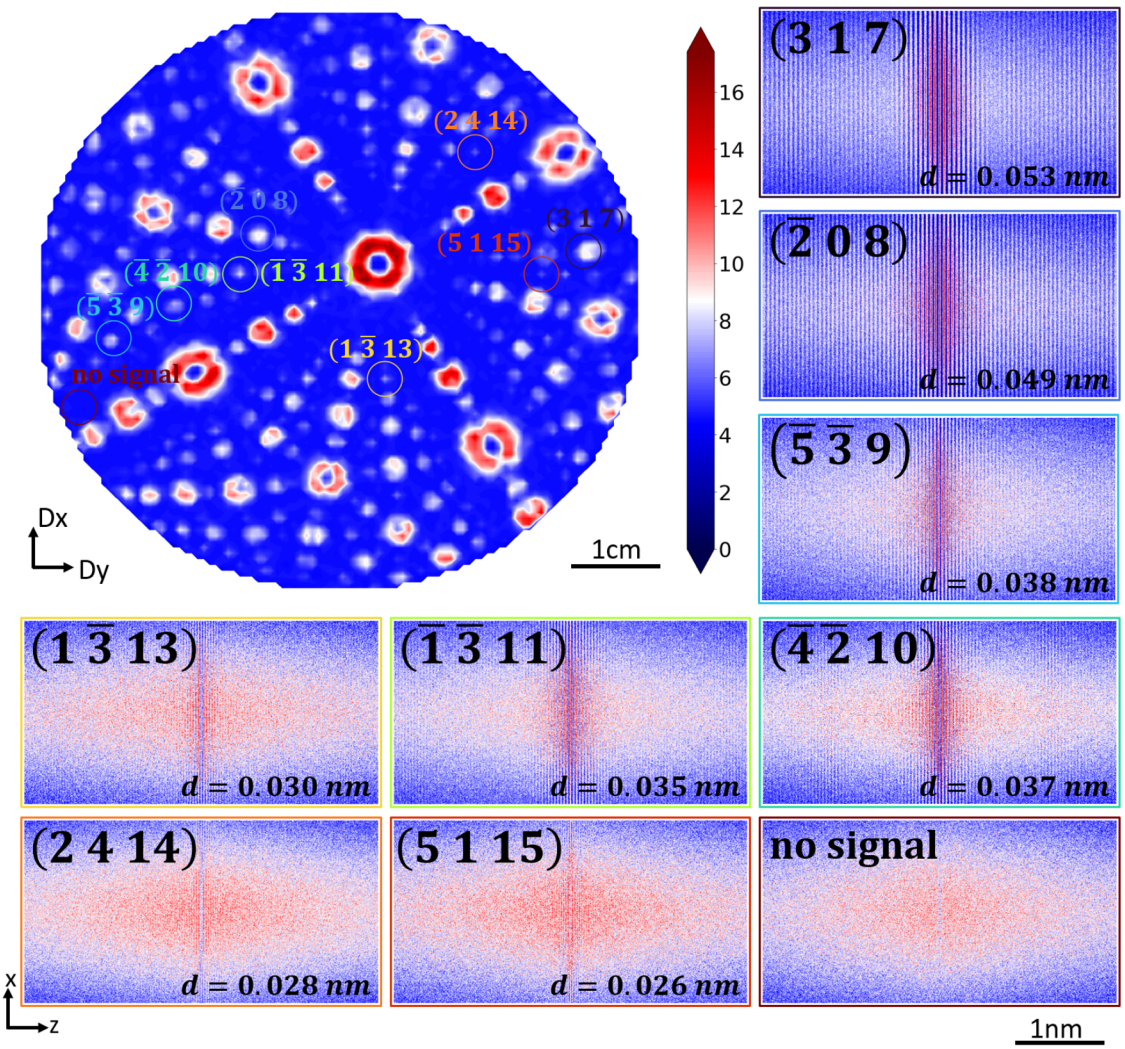


**FIG. 2.** Plane remnants in Al: Detector space map of the Fourier signal from an aluminum measurement. Each spot tags an atomic plane. SDMs of the data around the spot (encircled) reconstructed perpendicular to the surface are shown for selected spots/planes. Plane sets with a inter-plane spacing down to 26 pm are tagged correctly. Note that regions with no tag contain no images of planes.

given two plane sets on the detector to find the imaged angle needed for the ICF calculation and use the known angles between the same pair of crystal planes as the real angle to calculate the ICF for every pair of detected crystal planes. Second, we can use the known distance between the crystal planes and the number of planes found in any given slice to calculate the progression of the analysis along the depth axis for each slice. Third, we can calculate the volume occupied by the ions in each slice using the input parameter as aforementioned. Once the ICF is obtained, we can calculate the unique radius of the hemisphere that results in the calculated depth progression and occupied volume. Note that in this way we extract the actual radius of the hemisphere forming the tip's surface and not the width of the tip's cap as, e.g., measured by SEM images.[34] Hence, with respect to the reconstruction model in Ref. 19, the measured radius does not need to be adjusted and the tip-cap ratio is 1. This protocol follows the basic ideas introduced in Refs. 10 and 13. Note that being able to reveal the plane remnants consistently in small subsets of the full data set is essential to carrying out this procedure. Furthermore, note that the data gained from the one-dimensional FFT maps are fully sufficient to generate the reconstruction parameters and hence the process is time efficient. Finally, it is worth mentioning that revealing plane remnants in small subsets also enables the mapping of the crystallite orientations in nanocrystalline materials as discussed in Refs. 7 and 11.

In the following, we give a step-by-step description of how we automate the process described above starting from the signal maps

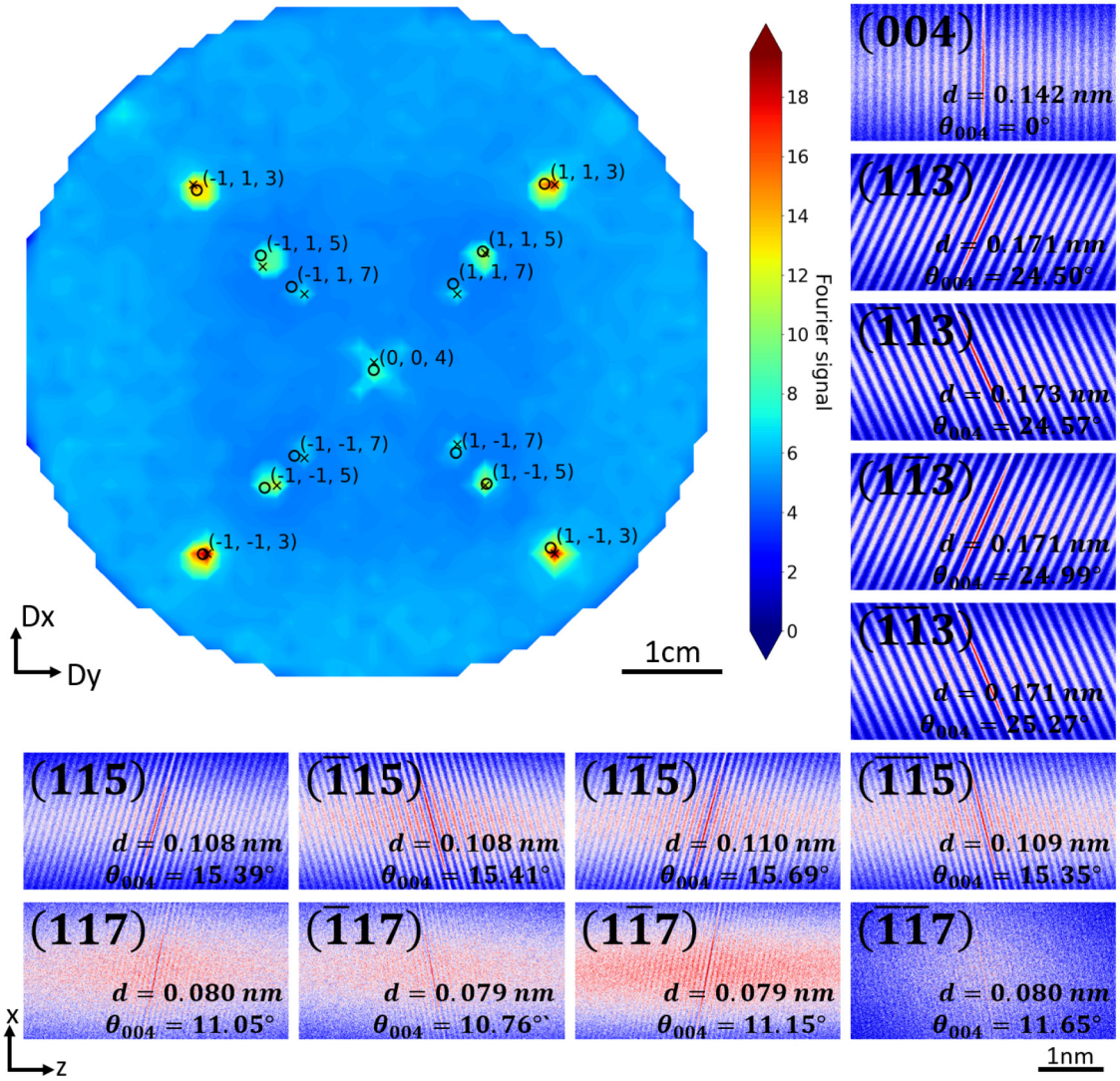


**FIG. 3.** Plane remnants in Ge: 13 plane sets found in a laser-assisted APT analysis of Ge. Overlapped to the FFT signal map (left) are the theoretical positions of the poles.[29] SDMs for all 13 plane sets are shown (right) together with the measured angles and plane distances. The expected plane distances are 0.142, 0.171, 0.109, 0.079 nm and the expected angles are 0, 25.24, 15.79, 11.24° for the {004}, {113}, {115} and {117} sets, respectively.[29] Details on how the SDMs are extracted from the signal map can be found in supplementary material Sec. S2.

shown in Figs. 1(d) and 2 for a laser-assisted APT analysis of a semiconductor heterostructure consisting of a 1.7 $\mu$m thick stack of SiGeSn/GeSn/Ge[35] containing approximately 450 millions ions.

A series of maps containing $5 \times 10^6$ ions and approximately 15–20 nm of depth progression per slice are shown in supplementary Fig. S10. We apply a 2D topological peak-search based on persistent homology[36] (see supplementary material, Sec. S1c) to each map to identify the peaks in the signal map. For convenience, a cluster search using the hierarchical linkage method in SciPy[27] or DBSCAN[37] is then used to group the peaks from all slices based on their detector position and the peak's position in FFT space (see supplementary material Fig. S11). The poles can now be either manually or automatically[38] matched to the respective crystal planes. Note that in future work the peaks and their relating plane sets should be labeled automatically slice by slice and then clustered based on their labeling. This would generate a fully automatic mapping of crystallite orientations in APT of multicrystalline materials.

It is now possible to calculate the ICF. As a result of the clustering of the plane signals, we know which remnant planes are present in each slice and at which position on the detector the respective plane is imaged. The angles between the crystal planes on the tip surface are known[29] and hence we can calculate the

implied ICF for each pair of crystal planes in each slice. The result of this calculation on the 1.7 $\mu$m thick stack of SiGeSn/GeSn/Ge is shown in supplementary material Fig. S12 for both slices of $3 \times 10^6$ and $5 \times 10^6$ ions using a $50 \times 50$ and a $60 \times 60$ Fourier grid, respectively (in Fig. S13 the point projection parameter $m + 1$[15] is shown for the same pairs of crystal planes). Note that the median values for the ICF are between 1.48 and 1.52 for all slices and over the whole depth. Collective outliers are caused by the fact that the tip surface is not a perfect hemisphere.[16] In order to avoid an effect of these outliers on the final reconstruction we choose to use the median ICF values as the "true" ICF in each slice. However, the ability to find and map the collective outliers could be used to inform reconstruction algorithms beyond the hemispherical constraint.[39]

The depth progression of the APT analysis in each slice can simply be inferred from the position of the peak in FFT space [see Fig. 1(c)] associated with the peaks on the signal map. We know the length of the DSR on which the FFT was carried out (the value was arbitrarily fixed to 10 as aforementioned). We know the distance between the plane sets in real space.[29] The position of the peak in FFT space [Fig. 1(c)] is directly associated to the plane spacing in the DSR for each identified plane set.[40] Hence, multiplying the length of the DSR by the expected plane spacing in real space and then dividing by the spacing measured via FFT gives the depth progression of the slice. This is equivalent to counting the number of planes in the DSR and multiplying it by the known plane spacing (adjusted for the angle under which the plane is imaged). This calculation can be done independently for each identified plane set in each slice. As shown in supplementary material Fig. S14 for the 1.7 $\mu$m thick stack of SiGeSn/GeSn/Ge, the process typically results in almost the same depth progression for all identified plane sets in all slices. The deviation between different plane sets is typically less than 1%. The exceptions are a few clearly visible outliers typically caused by the clustering step including noise peaks that have no physical relation to the underlying crystal planes in the cluster for the respective crystal plane.

As for the ICF, in order to avoid any influence of outliers on the reconstruction, we choose to use the median values as the "true" depth progression in each slice.

The radius of the tip can now be calculated. The ions contained within each slice are known and using the input parameters provided to the reconstruction,[15,19] we can calculate the overall volume that the ions occupy. We already know the depth progression contained in the slice and the ICF under which the slice is imaged. The ICF essentially tells us which part of the hemisphere is imaged on the detector. Finding the radius of the full hemisphere whose partial image on the detector results in the desired depth progression given the volume of the ions is now a simple geometrical problem that has a unique solution allowing us to infer the average radius of the hemisphere formed at the tip apex in each slice.

The radius evolution of the tip together with an image of the reconstructed data set and an elemental profile of the 1.7 $\mu$m thick stack of SiGeSn/GeSn/Ge is shown in Fig. 4(a). The radius evolution is shown for both slices of $3 \times 10^6$ and $5 \times 10^6$ ions which are in good agreement. In both cases, the expected "radius jumps" of the hemisphere at the interfaces between different materials[39] are captured by the calculation.

Figures 4(b) and 4(c) show the SDMs of the four {113} poles integrated over the entire 1.7 $\mu$m thick heterostructure. Note that the stack is almost lattice matched having a measured strain of 0.2 %[35] and hence the lattice constant is expected to be almost constant throughout the entire volume. All four {113} planes are readily visible in the SDMs and as shown in Fig. 4(c), the spread observed for a plane is approximately 0.14 nm and is symmetric for all four plane sets. This demonstrates that the reconstruction parameters extracted from the crystal plane remnants indeed result in a well-calibrated reconstruction over the entire volume.

## MEASURING LAYER THICKNESSES

A first application of the algorithm developed in this work is utilizing the crystal data to give an accurate estimate of the dimensions of a specific crystallite in a semiconductor heterostructure. This highlights the potential of this work for mapping of multicrystalline materials in three dimensions. Note that accurately estimating the dimensions of a subregion in an APT tomographs is not trivial.[20]

APT reconstructions of multi-layers calibrated via the crystal plane remnants are inherently giving faithful thickness estimates of all layers. This is due to the fact that the crystal planes are a reliable source for the calibration of the depth axis. In other words, if the distance between the crystal planes is reconstructed with a small error for all imaged planes over the whole multilayer, the depth axis must be calibrated accurately and hence the thicknesses must be correctly represented with a similarly small (relative) error.

However, we now show that the crystal plane remnants and the methods introduced here can be used to measure thicknesses of layers with an even higher precision. As an example, we use the thin GeSn layer that is shown in Fig. 3(a) at a depth of approximately 1275 nm. We define this layer to be extending between the crossing point of Si and Sn on one side and the point where the Sn concentration drops below 0.5 at. % on the other side. For the reconstruction shown in Fig. 3(a), this layer has an extension of exactly 18 nm.

The first method to precisely estimate the thickness is to simply filter out all the ions that are part of the layer based on the z-coordinates in the reconstruction shown in Fig. 3(a). We can now treat this set of ions as one (or multiple) slice(s) and calculate its (their) depth progression for each crystal plane found using the plane detection algorithm. In complete equivalence to finding the depth progression for the reconstruction data discussed in the previous section, we can deduce the depth progression generated by this set of ions and hence the thickness of the layer. Inside the GeSn layer we can find all four {113} poles (see Fig. S5) and the resulting depth measure is $17.80 \pm 0.07$ nm.

The second method again starts by filtering the ions contained in the layer based on the z-coordinates, and using them as one (or multiple) slice(s) for the plane finding algorithm. However, this time we progress to find all reconstruction parameters for the volume of the layer using the procedure described in the previous section. We can then reconstruct a local neighborhood around each

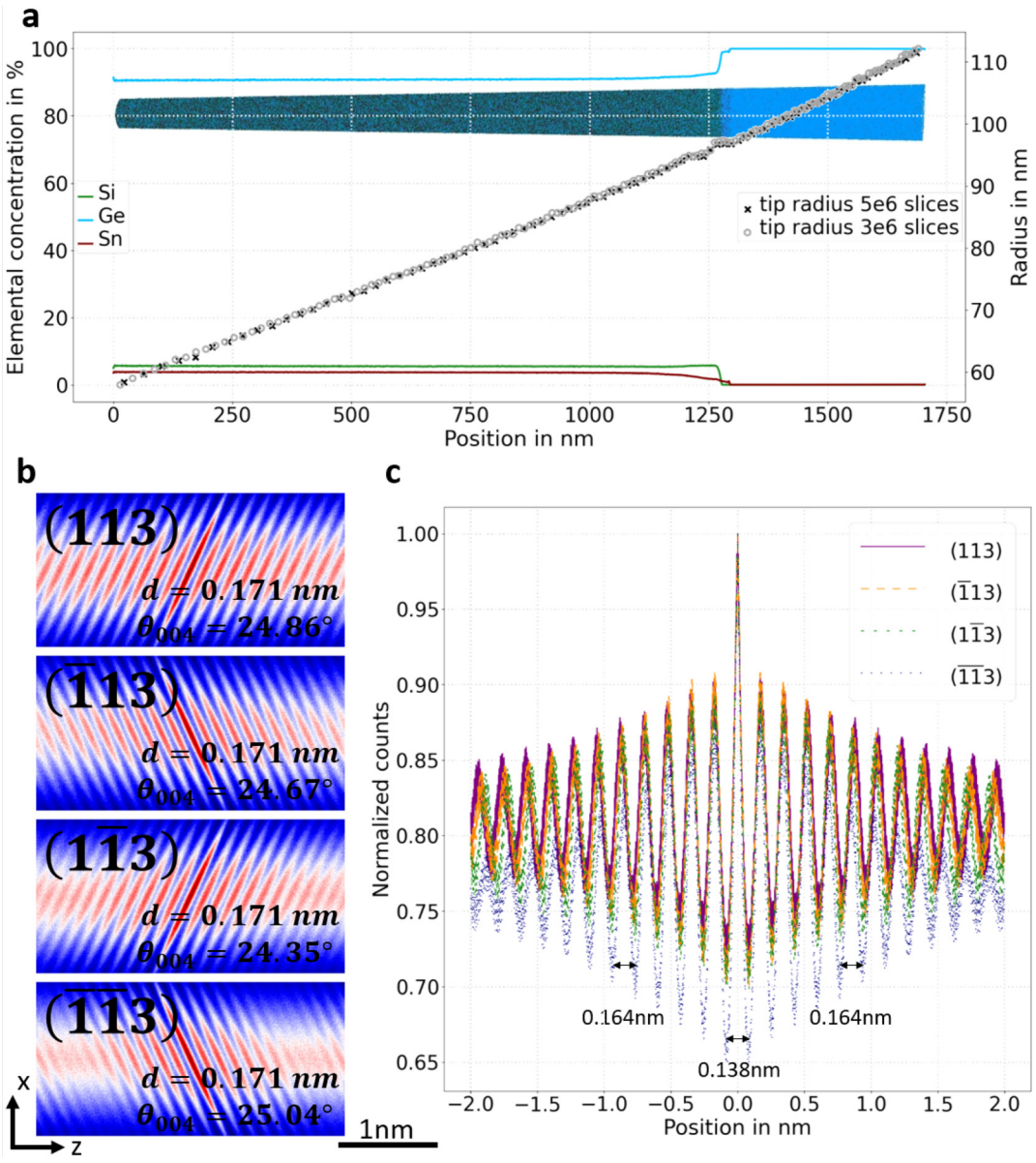


**FIG. 4.** Crystallographically guided reconstruction of a semiconductor heterostructure: Reconstructed data set, depth profile, and deduced radius progression of the sample (a). All 4 {113} are reconstructed using the radius progression and SDMs[12] are generated using all ions detected in the respective regions. Both the 2D (b) and 1D (c) SDM clearly show the respective {113} planes even when integrated over the full 1.7 $\mu$m thick stack of three different materials highlighting that the deduced radius progression creates a reliable depth progression and appropriate angle relations. The expected plane distance is 0.171 nm and the expected angle to the (004) pole is 25.24° (b). The overall spread of the imaged planes, meaning the aberrations acquired by reconstructing the full stack, is less than 0.14 nm for the main plane (c) and increases by only about 0.005 nm for every higher order neighbor plane.

crystal pole and measure the plane distances in these reconstructions using a discrete Fourier transform.[23] Multiplying the full length of the partial reconstruction with the known plane distance of the respective plane set and dividing by the measured distance, gives an accurate estimate of the overall thickness of the layer. Loosely speaking we simply count the number of crystal planes in the layer and use the known distance between these planes to estimate the thickness of the layer. Using the four {113} poles in the GeSn layer once more, we get a depth measure of 17.84 $\pm$ 0.16 nm in good agreement with the previous estimate.

## CONCLUSIONS

We have developed an efficient algorithm to find plane remnants in APT data starting from raw acquisition data. The algorithm finds patterns by applying a one-dimensional FFT to the z axis data of three-dimensional DSR of small neighborhoods of the full APT data sets. It can be successfully applied to a few million consecutively detected atoms at a time and hence allows the reliable and consistent extraction of plane remnants on slices of 10 nm or less along the tip axis/depth of an APT data set.

We have demonstrated that dynamic reconstructions of the APT data sets[13] are enabled by the detected atomic plane remnants and that the atomic planes can be used to extract accurate depth measures from APT data sets in semiconductor heterostructure, a long sought after goal in this field.[20,39]

The detailed information the plane remnant search provides particularly on metal tips can give new insights into the surface structure of APT tips that can be utilized to improve or calibrate new reconstruction algorithms[13,41] and to verify the validity of full-scale APT simulations.[30–32]

Finally, we believe that the algorithm introduced here will be of immense value for the emerging field of Atom Probe crystallography,[42] a field that aims to map the angular relations between different crystals in poly-crystalline and nanocrystalline,[7,8] alloys and the constitution of the respective grain boundaries.

## SUPPLEMENTARY MATERIAL

See the supplementary material for the parameter settings for the plane finding algorithm explained and additional output generated by the algorithm. Comprehensive looks at atomic planes found on Aluminum, Silicon, and SiGeSn are presented. Additional information with regard on how the plane finding algorithm can be utilize to extract reconstruction parameters from raw APT data are given and the relationship between the two most common projection parameters used in ATP—the image compression factor and the projection parameter—is laid out.

## ACKNOWLEDGMENTS

O.M. acknowledges support from NSERC Canada (Discovery, SPG, and CRD Grants), Canada Research Chairs, Canada Foundation for Innovation, Mitacs, PRIMA Québec, and Defense Canada (Innovation for Defense Excellence and Security, IDEaS). D.N.S and D.I. acknowledge support from the National Science Foundation (NSF DMR-0420532) and the Office of Naval Research (ONR N00014-04-0-0798, N00014-06-1-0539, N00014-09-1-0781, N00014-17-1-2870, and N00014-23-1-2593).

## AUTHOR DECLARATIONS

### Conflict of Interest

S. Koelling and O. Moutanabbir have a patent application related to the method presented in this paper.

### Author Contributions

**Sebastian Koelling:** Conceptualization (equal); Data curation (equal); Formal analysis (equal); Investigation (equal); Methodology (equal); Software (equal); Validation (equal); Visualization (equal); Writing – original draft (equal). **Simone Assali:** Project administration (supporting); Resources (equal); Writing – review & editing (equal). **Guillaume Nadal:** Data curation (supporting); Methodology (supporting); Software (supporting); Validation (supporting). **Dieter Isheim:** Resources (equal); Writing – review & editing (equal). **David N. Seidman:** Resources (equal); Writing – review & editing (equal). **Oussama Moutanabbir:** Funding acquisition (lead); Project administration (lead); Supervision (lead); Writing – original draft (supporting); Writing – review & editing (equal).

## DATA AVAILABILITY

The data that support the findings of this study are available from the corresponding author upon reasonable request.

## REFERENCES

[1] S. J. Billinge and I. Levin, Science **316**, 561 (2007).
[2] J. S. Langer, Rev. Mod. Phys. **52**, 1 (1980).
[3] M. A. Meyers, A. Mishra, and D. J. Benson, Prog. Mater. Sci. **51**, 427 (2006).
[4] A. S. Eggeman, R. Krakow, and P. A. Midgley, Nat. Commun. **6**, 7267 (2015).
[5] J. Miao, T. Ishikawa, I. K. Robinson, and M. M. Murnane, Science **348**, 530 (2015).
[6] J. Miao, P. Ercius, and S. J. Billinge, Science **353**, 1380 (2016).
[7] P. V. Liddicoat *et al.*, Nat. Commun. **1**, 1 (2010).
[8] M. Herbig *et al.*, Phys. Rev. Lett. **112**, 126103 (2014).
[9] C. Wang *et al.*, Matter **3**, 1999 (2020).
[10] B. Gault *et al.*, J. Appl. Phys. **105**, 034913 (2009).
[11] A. Breen, A. Day, B. Lim, W. Davids, and S. Ringer, Ultramicroscopy **243**, 113640 (2023).
[12] B. P. Geiser, T. F. Kelly, D. J. Larson, J. Schneir, and J. P. Roberts, Microsc. Microanal. **13**, 437 (2007).
[13] B. Gault *et al.*, Ultramicroscopy **111**, 1619 (2011).
[14] B. Gault *et al.*, Nat. Rev. Methods Primers **1**, 1 (2021).
[15] P. Bas, A. Bostel, B. Deconihout, and D. Blavette, Appl. Surf. Sci. **87**, 298 (1995).
[16] F. Vurpillot, A. Bostel, and D. Blavette, J. Microsc. **196**, 332 (1999).
[17] S. Koelling *et al.*, Nano Lett. **13**, 2458 (2013).
[18] D. Blavette, E. Cadel, A. Fraczkiewicz, and A. Menand, Science **286**, 2317 (1999).
[19] D. J. Larson, T. Prosa, R. M. Ulfig, B. P. Geiser, and T. F. Kelly, *Local Electrode Atom Probe Tomography* (Springer, 2013).
[20] S. Koelling *et al.*, Appl. Phys. Lett. **95**, 144106 (2009).
[21] B. Deconihout, P. Gerard, M. Bouet, and A. Bostel, Appl. Surf. Sci. **94**, 422 (1996).
[22] N. D. Wallace, A. V. Ceguerra, A. J. Breen, and S. P. Ringer, Ultramicroscopy **189**, 65 (2018).
[23] F. Vurpillot, G. Da Costa, A. Menand, and D. Blavette, J. Microsc. **203**, 295 (2001).
[24] L. Yao *et al.*, Ultramicroscopy **111**, 458 (2011).
[25] J. W. Cooley and J. W. Tukey, Math. Comput. **19**, 297 (1965).
[26] C. R. Harris *et al.*, Nature **585**, 357 (2020).
[27] P. Virtanen *et al.*, Nat. Methods **17**, 261 (2020).
[28] B. Gault *et al.*, Appl. Phys. Lett. **95**, 034103 (2009).
[29] S. H. Simon, *The Oxford Solid State Basics* (OUP Oxford, 2013).
[30] C. Oberdorfer, S. M. Eich, and G. Schmitz, Ultramicroscopy **128**, 55 (2013).
[31] N. Rolland, F. Vurpillot, S. Duguay, and D. Blavette, Microsc. Microanal. **21**, 1649 (2015).
[32] C. Fletcher, M. P. Moody, and D. Haley, J. Phys. D: Appl. Phys. **53**, 475303 (2020).
[33] D. Brandon, J. Sci. Instrum. **41**, 373 (1964).

[34]A. Shariq *et al.*, Ultramicroscopy **109**, 472 (2009).
[35]S. Assali *et al.*, J. Appl. Phys. **132**, 195305 (2022).
[36]N. Otter, M. A. Porter, U. Tillmann, P. Grindrod, and H. A. Harrington, EPJ Data Sci. **6**, 1 (2017).
[37]M. Ester, H.-P. Kriegel, J. Sander, X. Xu *et al.*, *KDD'96: Proceedings of the Second International Conference on Knowledge Discovery and Data Mining* (1996), pp. 226–231.
[38]T. Britton *et al.*, Mater. Charact. **117**, 113 (2016).
[39]N. Rolland *et al.*, Microsc. Microanal. **23**, 247 (2017).
[40]B. G. Osgood, *Lectures on the Fourier Transform and Its Applications* (American Mathematical Soc., 2019). Vol. 33.
[41]D. Beinke and G. Schmitz, Microsc. Microanal. **25**, 280 (2019).
[42]B. Gault, M. P. Moody, J. M. Cairney, and S. P. Ringer, Mater. Today **15**, 378 (2012).